The Astrophysical Journal, 688:656–668, 2008 November 20

CORONAL ROTATION AT SOLAR MINIMUM FROM UV OBSERVATIONS

S. Giordano and S. Mancuso
INAF-Osservatorio Astronomico di Torino, via Osservatorio 20, 10025, Pino Torinese (To), Italy; giordano@oato.inaf.it
Received 2007 April 24; accepted 2008 July 7

ABSTRACT

The observations of the UVCS *SOHO* instrument from 1996 May to 1997 May have been analyzed to reconstruct intensity time series of the O VI 1032 Å and H I Lyα 1216 Å spectral lines at different coronal heliolatitudes from 1.5 to 3.0 $R_\odot$ from Sun center. At solar minimum, some features persist for several rotations, thus allowing analysis of the UV emission as time series modulated at the period of the solar rotation. We find evidence of coronal differential rotation, which significantly differs from that of the photospheric plasma. The estimated equatorial synodic rotation period of the corona at 1.5 $R_\odot$ is 27.48 $\pm$ 0.10 days. The study of the latitudinal variation shows that the UV corona decelerates toward the photospheric rates from the equator up to the poleward boundary of the midlatitude streamers, reaching a peak of 28.16 $\pm$ 0.20 days around +30° from the equator at 1.5 $R_\odot$, while a less evident peak is observed in the northern hemisphere. This result suggests a real north-south rotational asymmetry as a consequence of different activity and weak coupling between the magnetic fields of the two hemispheres. The study of the radial rotation profiles shows that the corona is rotating almost rigidly with height, but we find an abrupt increase by about half a day between 2.3 and 2.5 $R_\odot$. The larger gradients of the rotation rates are localized at the boundaries between open and closed field lines, suggesting that in these regions the differential rotation might be a source of magnetic stress and, consequently, of energy release.

Subject headings: Sun: corona — Sun: rotation — Sun: UV radiation

Online material: color figures

1. INTRODUCTION

The rotation of the solar corona in the minimum phase of the solar cycle differs from what is observed on the photosphere and chromosphere in that, away from the equator, the corona tends to rotate faster and more rigidly than photospheric plasma. Consequently, the differential rotation of the corona is observed to be much less pronounced than in the photosphere. Previous investigations have mainly focused their analyses on observations of the coronal rotation in white light (Hansen et al. 1969; Fisher & Sime 1984), the Fe XIV green line (Antonucci & Svalgaard 1974), microwave (Aschwanden et al. 1995), and X-ray (Weber et al. 1999) and through extrapolation of photospheric data (Hoeksema & Scherrer 1987; Antonucci et al. 1990). More recently, the rotation of the inner and outer corona at solar minimum has been investigated by Lewis et al. (1999) and Stenborg et al. (1999) using Fe XIV and white-light data from the Large Angle Spectrometric Coronagraph (LASCO) aboard the *Solar and Heliospheric Observatory* (*SOHO*) spacecraft. However, at present, there have been no rotation studies that make extensive use of ultraviolet (UV) emission lines. In UV, coronal rotation rates can be inferred, thanks to the regular occurrence of localized coronal features that, being much brighter than the background corona, act as tracers whenever they have sufficient stability to reappear at the same limb for several rotations. The measurement of the rotation of the extended corona can thus be achieved by using regular synoptic observations obtained with the Ultraviolet Coronagraph Spectrometer (UVCS) instrument on *SOHO*, which is able to provide long and uninterrupted time series of data ranging from about 1.5 to 3.0 $R_\odot$ from Sun center. These studies are of particular importance in that there are still several open questions about how the photospheric differential rotation is transferred into the corona and on the rotation rate of different coronal features (in particular the small-scale structures). The investigation of the rotation rate of the solar corona is especially interesting, because the interaction between the differentially rotating photosphere and the near-rigid rotating corona could be a possible energy source for both coronal heating and solar wind acceleration and, consequently, may provide a powerful constraint on solar wind models.

The purpose of this paper is to describe the latitudinal and radial dependence of the coronal rotation rate during solar minimum conditions, based on the analysis of the available daily observations made with the UVCS instrument from 1996 mid-May to 1997 mid-May. The latitudinal range of our data extends from the solar equator to about 30° north and south with respect to the poles, with enough spatial resolution to search for the latitudinal dependence of the rotation rates. The plan of this paper is as follows. In § 2, we describe the data selection and reduction and outline the different steps in our analysis. In § 3, we give a brief description of the two methods (Lomb-Scargle periodogram and autocorrelation techniques) that have been applied for the analysis of the time series data. In § 4, we present our results, discussing the observed radial and latitudinal variations and the north-south rotational asymmetry separately. Finally, after a brief discussion, we summarize our conclusions in § 5.

2. OBSERVATIONS AND DATA REDUCTION

The UVCS instrument aboard *SOHO* is an internally and externally occulted coronagraph consisting of two spectrometric channels for the observation of spectral lines in the UV range and a visible light channel for polarimetric measurements of the extended solar corona. The UVCS slit is perpendicular to the sunward direction on the plane of the sky and can be moved along the radial direction to observe the solar corona between 1.4 and 10 $R_\odot$ with a field of view of 40′. In order to cover all the possible position angles, the slit can be rotated by 360° about an axis pointing to the center of the Sun. For a complete description of the UVCS instrument, see Kohl et al. (1995).

In this work, we present a coronal rotation study that makes use of data acquired by the UV channel that is optimized for the observation of the O VI 1032 Å spectral line. The UV channel, optimized for the observation of the H I Lyα 1216 Å line will be used only to validate our results at midlatitudes. We focus our investigation on the period of minimum of solar activity, when the solar corona is relatively stable, with a quasi-dipole axisymmetric global magnetic field configuration, and coronal structures are sufficiently long lived. In particular, we selected a 1 year observation period, from 1996 mid-May to 1997 mid-May, in order to better compare our results with an analogous study of the solar coronal rotation carried out by Lewis et al. (1999) that was obtained by analyzing the images acquired during the same period by both LASCO C1 (Fe XIV green coronal emission line) and C2 (white light) telescopes. We must emphasize that UVCS observations are complementary to LASCO measurements in that the two telescopes are sensitive to different coronal parameters. In fact, while the white-light broadband images from LASCO C2 are sensitive only to the electron density along the line of sight and the Fe XIV line emission can occur only above active regions, where the electron temperature is about 1.5×10^6 K, the O VI 1032 Å spectral line emissivity depends on temperature, density, and outflow speed. In the time interval of interest for this work, UVCS ran a counterclockwise daily synoptic observation program, which covered the full corona from 1.5 to 3.0 $R_\odot$ at eight different roll angles separated by an angular step of 45°. Complementary special observations were also included in our study whenever the pointing was the same as the synoptic program. On average, the cadence of the data was about 1 per day, although unevenly spaced in time, with only a small number of gaps due to telemetry problems or special spacecraft maneuvers. In this way, the UVCS observation program yields a powerful tool that allows studying the rotation of the UV corona during the minimum of solar activity from a very complete, discrete, but almost continuous set of data. For instance, with the UVCS mirror pointed to 90° counterclockwise from north pole at the distance of 1.5 $R_\odot$, a set of 349 data is available (out of 1 year of data), which represents an average time coverage of about 95%. Even with the mirror pointed to 225°, at the distance of 1.75 $R_\odot$, which is the worst available case, we still have a time coverage of about 86%.

An outline of the UVCS synoptic observation plan is shown in Figure 1, where the solid straight lines represent the pointing of the UVCS slit positions relative to the Sun corresponding to the observations under study. The instrument rolls analyzed in this work were those positioned at the midlatitude regions (45°, 135°, 225°, and 315°) and at the equatorial regions (90° and 270°). The slit distances from the Sun center were 1.5, 1.75, and 2.0 $R_\odot$ for the midlatitude regions and 1.5, 1.7, 1.9, 2.2, 2.6, and 3.0 $R_\odot$ for the equatorial regions. Equatorial distances higher than 2.0 $R_\odot$ have been analyzed only to study the radial variation of the rotation rate, since the low count rates at these heliocentric distances did not allow a latitudinal variation study. The raw UVCS data for the time interval of interest are available online from the SOLAR archive (Cora et al. 2003) at the INAF/OATo Web site.[1] The data have been calibrated by using the most recent release of the UVCS Display and Analysis Software (ver. 40, available at the UVCS Web site[2]), which also takes into account the time variations of the instrument performances. All the subsequent exposures with the same mirror pointing were summed together, so that the average exposure time of the time series elements is 670 s. For each selected roll angle, we used the data acquired in a ±850″

[1] See http://solar.oato.inaf.it.
[2] See http://cfa-www.harvard.edu/uvcs.

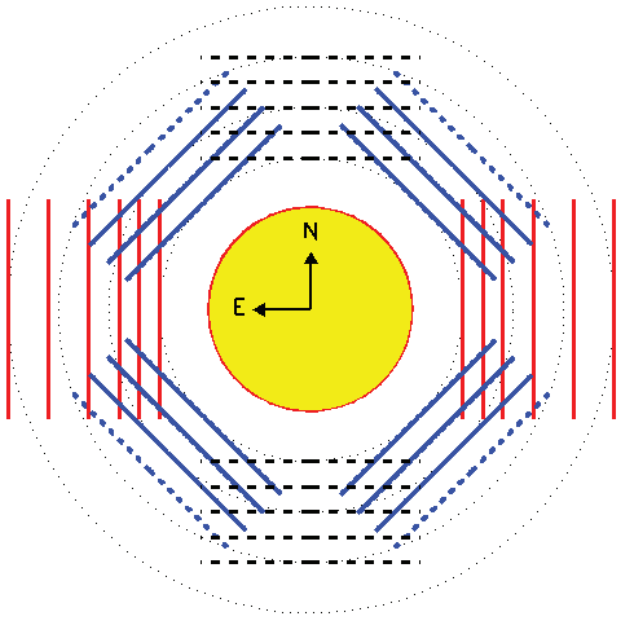

FIG. 1.—Coronal heights and polar angles observed with the UVCS synoptic program in the time interval from 1996 mid-May to 1997 mid-May. Red and blue straight lines display, respectively, the UVCS slit positions relative to the Sun corresponding to the equatorial and midlatitude observations analyzed in this work.

range around the center of the slit, and, in order to increase the statistics, we further rebinned the data to 21 spatial elements along the slit for each observation, thus reducing the spatial resolution along the slit to ≃81″, which corresponds to a latitude step of about 3.2° at 1.5 $R_\odot$ and 2.4° at 2.0 $R_\odot$. We restricted our analysis to a latitudinal range of about ±60° around the equator, where the signal-to-noise ratio was found to be high enough for a reliable period determination. This is also the region over which bright streamer structures are most visible during the minimum of solar activity.

We must point out that, because of instrumental effects, such as a cross talk effect among the two UVCS gratings and the mirror mechanisms or the variable width of the spectrometer slit, the effective observed distances can be different by a few percent from the nominal mirror pointings mentioned above (see Table 1) and may change at the time the mechanisms positions are varied. However, we verified that in the period of interest the drift of the pointing was fairly constant, because the UVCS mechanisms were quite stable in the first year of observations. Moreover, we should emphasize that the observed distances (projected into the plane of the sky) are not constant along the slit. For example, for a nominal mirror pointing at 1.50 $R_\odot$ in the selected ±850″ range around the center of the slit, the actual observed distance ranges from 1.48 ± 0.02 $R_\odot$ at the slit center to as much as 1.70 ± 0.02 $R_\odot$ at the edges of the slit. For completeness, the actual observed distances at the center and at the edges of the slit are reported in Table 1 for the different mirror roll angles.

In order to estimate the total intensity of a selected spectral line from each coronal region element, the calibrated and combined UVCS spectra were fitted with a function resulting from the convolution of a Gaussian function (for the coronal spectral profile), with a Voigt curve describing the instrumental broadening and a function accounting for the width of the slit (Giordano 1998). All the data in the period under study were collected and used to build the intensity synoptic maps at a fixed mirror pointing. In the top panel of Figure 2, we show the O VI 1032 Å intensity synoptic map obtained with the UVCS mirror pointed

TABLE 1
SUMMARY OF OBSERVED HEIGHTS

Mirror[a] ($R_\odot$)	Slit Center[b] ($R_\odot$)	Slit Edges[c] ($R_\odot$)
Midlatitudes Roll		
1.50	1.48	1.70
1.75	1.78	1.97
2.00	2.06	2.23
Equatorial Roll		
1.50	1.48	1.70
1.70	1.71	1.91
1.90	1.95	2.12
2.20	2.29	2.44
2.60	2.73	2.86
3.00	3.17	3.28

[a] Nominal mirror pointing.
[b] Effective observed height at the slit center.
[c] Effective observed height at the slit edges.

at 1.5 $R_\odot$. Similar images have been built at all the observed heights. Indeed, the intensity map of Figure 2 shows a clear modulation, which can be readily attributed to the rotation of persistent features through several consecutive rotations. Previous studies (e.g., Fisher & Sime 1984) have shown that large-scale features are actually seen to persist for several synodic rotations. Consequently, the intensity at a fixed location in the synoptic O VI 1032 Å image yields a suitable time series for the analysis period.

Unfortunately, although the H I Lyα data have been also reduced for this study, they were found, in general, less reliable for a rotation period analysis, especially in an extended portion around the streamer belt region. In fact, although an image similar to the one presented in the top panel of Figure 2 has also been built from H I Lyα observations (see Fig. 2, *bottom*), it presents a more diffuse and constant signal from the streamer belt. This is probably due a concurrence of effects, such as the higher diffusion of the light H atoms, the different relative abundances of the H and O atoms in the streamer belt, and the different sensitivity of the O VI and Lyα spectral lines to the electron density along the line of sight (Noci et al. 1997). Since the H I Lyα data were found to be less reliable for a thorough coronal rotation period study in the equatorial region, they will be used only for validating the rotation period results at midlatitudes.

3. METHODOLOGY

This section describes the two methods used for the analysis of the time series data for coronal rotation. Different time series analysis methods can be applied to determine the data periodicity, all with strengths and limits depending on the data type and on the goals of the analysis. Since the Lomb-Scargle periodogram technique is able to deal with unevenly spaced data, we used this latter technique as our main investigation tool for the analysis of the coronal period. In order to validate our results and obtain an independent period determination, we also used the autocorrelation analysis technique, applied over data interpolated onto an equally spaced grid.

3.1. *Period Determination by the Lomb-Scargle Periodogram Technique*

From UVCS data, we built, as described in the previous paragraphs, the O VI 1032 and H I Lyα intensity time series at each position along the instrumental slit for a selected time window.

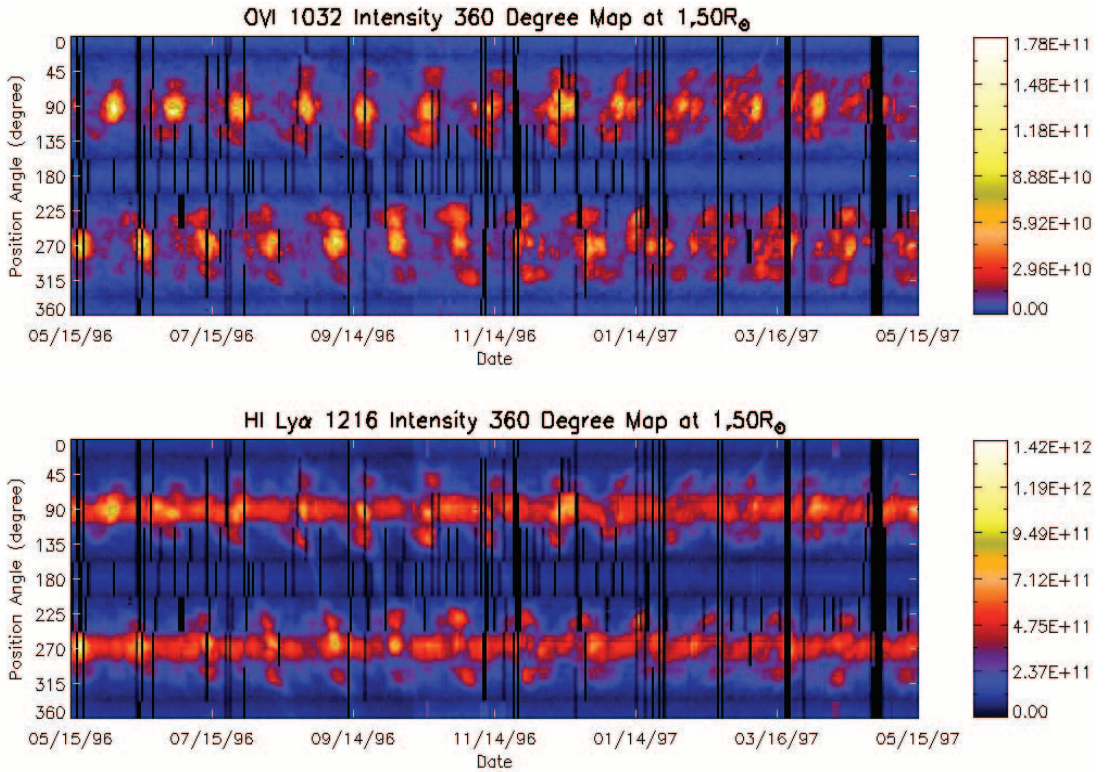

FIG. 2.—O VI 1032 Å (*top*) and H I Lyα 1216 Å (*bottom*) intensity synoptic maps in the time interval from 1996 mid-May to 1997 mid-May, corresponding approximately to Carrington rotations from 1909 to 1922. The intensities are measured in photons $cm^{-2}\ s^{-1}\ sr^{-1}$. Position angles, measured counterclockwise from the north pole, increase from top to bottom and cover a full 360° of latitude at 1.50 $R_\odot$.

The power spectrum analysis was carried out by means of the Lomb-Scargle periodogram technique (Lomb 1976; Scargle 1982). As already mentioned, the main advantage of this approach is that the normalized Lomb-Scargle periodogram is designed to study periodicities from unevenly sampled data. For a given position along the slit, s, and observation time, t_i, which corresponds to the middle of the integration time interval, if we denote the intensity time series by $y_s(t_i)$ for $i = 1, \ldots, N$, where N is the number of observations, the mean and the total variance of the data are given, respectively, by

$$\bar{y}_s = \frac{1}{N}\sum_{i=1}^{N} y_s(t_i), \tag{1}$$

$$\sigma_s^2 = \frac{1}{N-1}\sum_{i=1}^{N}[y_s(t_i) - \bar{y}_s]^2. \tag{2}$$

Unlike Fourier analysis, in which Fourier frequencies are used, we assume that there are M test frequencies $f_1, f_2, \ldots, f_M$, with corresponding angular frequencies $\omega_j = 2\pi f_j$ and periods $T_j = 1/f_j$ for $j = 1, \ldots, M$. Assuming that ΔT is the total length of the observing interval, the test frequencies are chosen regularly spaced in the range from $\omega = 2\pi/\Delta T$, which corresponds to just one cycle in the data, to $\omega = \pi N/\Delta T$, which is the traditional Nyquist frequency for evenly spaced data. The Lomb-Scargle periodogram, normalized by the total variance of the data σ_s^2, is defined in Press & Rybicki (1989) as

$$P_s(\omega_j) = \frac{1}{2\sigma_s^2}\left(\frac{\left\{\sum_{i=1}^{N}[y_s(t_i) - \bar{y}_s]\cos[\omega_j(t_i - \tau_j)]\right\}^2}{\sum_{i=1}^{N}\cos^2[\omega_j(t_i - \tau_j)]} + \frac{\left\{\sum_{i=1}^{N}[y_s(t_i) - \bar{y}_s]\sin[\omega_j(t_i - \tau_j)]\right\}^2}{\sum_{i=1}^{N}\sin^2[\omega_j(t_i - \tau_j)]}\right), \tag{3}$$

where τ_j is defined by

$$\tan(2\omega_j\tau_j) = \frac{\sum_{i=1}^{N}\sin(2\omega_j t_i)}{\sum_{i=1}^{N}\cos(2\omega_j t_i)}. \tag{4}$$

The choice of M depends on the number of independent frequencies N_0. Horne & Baliunas (1986) performed extensive Monte Carlo simulations to investigate the relationship between M and N_0, giving a simple least-squares formula to estimate N_0 from the number of observations N in a time series:

$$N_0 \approx -6.362 + 1.193N + 0.00098N^2. \tag{5}$$

This empirical formula is adequate for most purposes by actually taking M as N_0 (Press et al. 2007). In our case, this choice is supposed to be valid also, because there is no important data clumping. In fact, although the data are irregularly spaced, we have approximately one measurement per day and rarely more than one measurement in a single day.

This spectral power estimate has several useful properties. For a given frequency ω_j, the τ_j term makes the periodogram invariant to time shifting. Moreover, this formulation is exactly equivalent to a linear least-squares fit of a sinusoid of given frequency ω to the time series data,

$$y(t) = A_\omega \sin(\omega t - \phi_\omega) + B_\omega. \tag{6}$$

An important property of the Lomb-Scargle normalized periodogram $P_s(\omega)$ is that whenever the time series is sampled by a pure Gaussian noise, the periodogram ordinate at each frequency follows an exponential probability distribution (Scargle 1982). That is, the probability that the periodogram for any sampled frequency is of height z or higher is e^{-z}. If z is the maximum value in the spectrum that scans M independent frequencies, then the probability that each frequency is smaller than z is $1 - e^{-z}$, and so the probability that every frequency is lower than z is $(1 - e^{-z})^M$. This is the probability that the data contain a signal (Horne & Baliunas 1986). Therefore, the observed statistical significance level for testing the null hypothesis that such a peak is due to chance is given by

$$F = 1 - (1 - e^{-z})^M. \tag{7}$$

This value is also called the false-alarm probability of the null hypothesis. In other words, the computed periodogram tests the hypothesis that the time and intensity populations represent a significant periodic signal at a given frequency against the hypothesis that they represent random noise.

The frequency analysis was performed on the natural logarithm of the data in order to compress their dynamic range (which is about 2 orders of magnitude) and reduce the impulsive effects on the time series due to the recurrence of active region streamers. This procedure allowed us to obtain a more sinusoid-like signal (e.g., Weber et al. 1999) and to stabilize the data variance (e.g., Box & Cox 1964). In order to remove possible long-term variations or trends due to the changing Sun-*SOHO* distance or uncorrected instrumental effects, the analyzed time series analyzed were detrended by subtracting a linear fit to the intensity data. In Figure 3, we report an example of the O VI 1032 Å intensity time series observed in the east equatorial region (90° counterclockwise from the north pole) at 1.5 $R_\odot$ (*top*), the modified time series (*middle*), and the relative power spectrum from the Lomb-Scargle periodogram analysis (*bottom*). In order to enhance the spectral resolution and to avoid missing the peak of the spectral signal, we oversampled by a factor of 4 the periodogram test frequencies in the region around the main peak, as suggested, for example, by Press et al. (2007). Finally, in order to define more precisely the values of the rotation period, we performed a cubic interpolation of the periodogram in the spectral region around the main peak. This method closely approximates the theoretically "sinc" interpolation function using cubic polynomials (e.g., Park & Schowengerdt 1983). Having $N = 349$ observations and $M = 529$ test frequencies (from eq. [5]), the 0.001 significance level, which means 0.1% false-alarm probability, corresponds to a peak of value $z = 13.17$. Although the significance level of the power peaks, computed by equation (7), depends on the estimated number of independent frequencies (see eq. [5]), we verified that, with a very conservative assumption ($M = N/2$), we obtain a 0.1% false-alarm probability at the power value $z = 12.06$. Since the peak corresponding to a period of 27.46 days has a z-value $\approx$96, then the false-alarm probability is thus negligible. A second example of intensity time series and period analysis is shown in Figure 4 for data taken at 120° counterclockwise from north pole at 1.5 $R_\odot$. In our analysis, we included only those data that yielded periods with false-alarm probability lower than 0.1%.

The uncertainty on the frequency determination was evaluated following the Horne & Baliunas (1986) formulation,

$$\sigma_f = \frac{3\sigma_n}{4\sqrt{N}\Delta TA}\ \left(\mathrm{s}^{-1}\right), \tag{8}$$

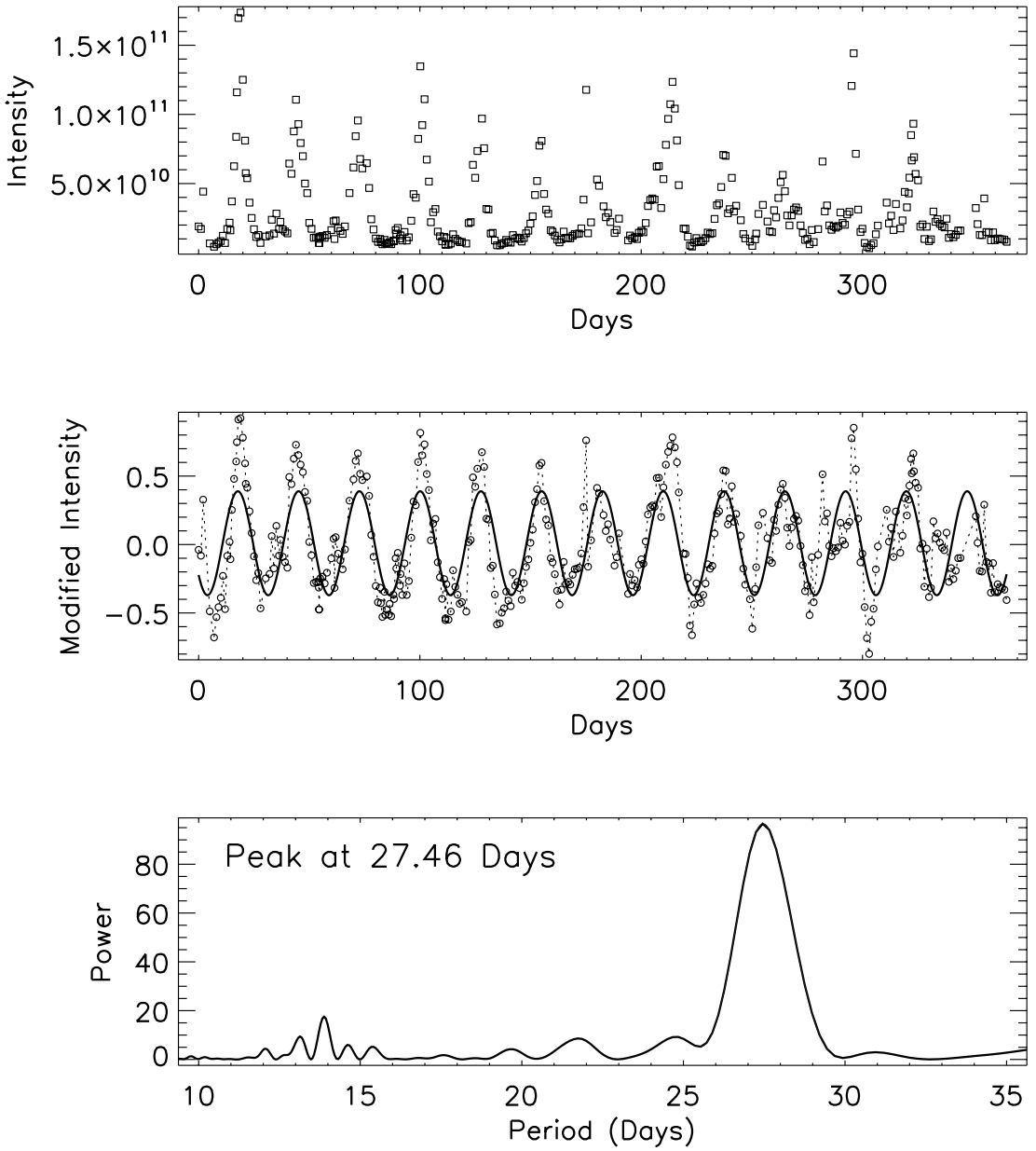

FIG. 3.—*Top*: O VI 1032 Å intensity time series at 90° from the north pole at the heliocentric distance of 1.5 $R_\odot$. *Middle*: Modified data and, superimposed, the computed sinusoidal signal with a period of 27.46 days determined from the main peak of the power spectrum shown in the bottom plot. We see also the appearance of a peak corresponding to half the main rotation rate (around 13.75 days) due to a harmonic of the main peak. [*See the electronic edition of the Journal for a color version of this figure.*]

where σ_n^2 is the variance of the residual after subtracting the least-squares fitted sine curve (see eq. [6]), ΔT is the total length of the observing interval, and A is the amplitude of the signal obtained from a least-squares fit to the data of a sinusoidal curve with a frequency equal to the peak frequency. Therefore, the uncertainty on the period determination from the Lomb-Scargle periodogram technique is

$$\sigma_T = \frac{\sigma_f}{f^2} \text{ (s)}. \tag{9}$$

In the case of the two time series shown in Figures 3 and 4, we have period uncertainties of about 0.11 days, while for noisier time series (higher distances and latitudes), the uncertainties reach up to 0.30 days. A significance assessment of the periods found in the periodogram analysis can be done via Monte Carlo methods (e.g., Horne & Baliunas 1986; Peterson et al. 1998; Ranucci 2006). We thus designed and ran extensive Monte Carlo simulations for the time series reported in Figures 3 and 4, and, as described in the Appendix, we verified that the quoted periodicities are not artifacts of the sampling and noise. We also determine with this independent method that the period uncertainties of these data series are of the order of 0.1 days. We finally verified that the Lomb-Scargle periodogram analysis on the unmodified data (that is, without "detrend" and logarithmic transformation) provides period results that are not significantly different, within the error bars, as clearly shown in Table 2.

Above 2 $R_\odot$, where the statistics are less reliable, the period estimates were found to be affected by a low periodic signal significancy and large uncertainties, and therefore they were not included

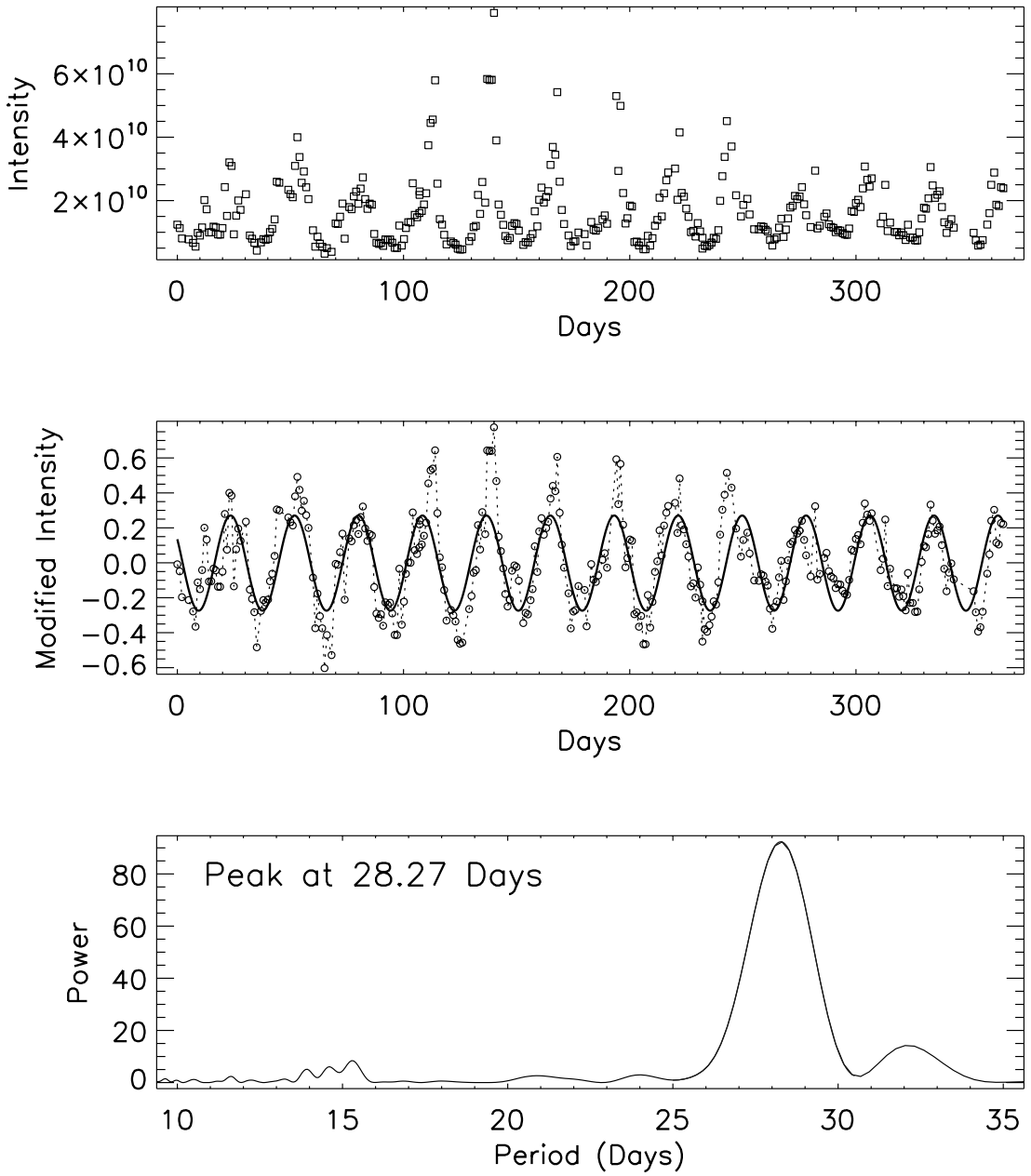

FIG. 4.—*Top*: O VI 1032 Å intensity time series at 120° from the north pole at the heliocentric distance of 1.5 $R_{\odot}$. *Middle*: Modified data and, superimposed, the computed sinusoidal signal with a period of 28.27 days determined from the main peak of the power spectrum shown in the bottom plot. The peak at period around 32 days is not significant, because of the high false-alarm probability (see the Appendix for a detailed discussion). [*See the electronic edition of the Journal for a color version of this figure.*]

in this work. Although we treated the east and west limbs independently, we finally performed a weighted average of the rotation periods from both limbs, with errors estimated by means of weighted standard deviations. We note that an apparent lack of symmetry between the east and west limb, also mentioned by Lewis et al. (1999), is a somewhat puzzling and important source of uncertainty in our period determination. This asymmetry might be tentatively attributed to a viewing effect arising from the inclination of the magnetic field axis with respect to the rotation one (Wang et al. 1997; Mancuso & Garzelli 2007).

TABLE 2
PERIOD RESULTS

Time Series Polar Angle (deg)	Unmodified Data Period (days)	Modified Data Period (days)
90	27.46 ± 0.11	27.54 ± 0.11
120	28.27 ± 0.13	28.16 ± 0.12

3.2. *Period Determination by Autocorrelation Technique*

In order to double-check our results, we derived a different estimate of the mean synodic rotation period of the UV corona between about 1.5 and 2 $R_{\odot}$ by using the autocorrelation technique over the same data set. This technique has been extensively applied in previous studies of coronal rotation (e.g., Parker et al. 1982; Sime et al. 1989; Lewis et al. 1999). The autocorrelation function (ACF) measures the degree of linear correlation between

a time series and the same time series delayed or lagged by a number of days. The ACF at lag k for a given time series $y_s(t_i)$ with $k = 0, 1, \ldots, N$, is defined as

$$\mathrm{ACF}(k) = \frac{\sum_{i=0}^{N-k-1}[y_s(t_i) - \bar{y}_s][y_s(t_{i+k}) - \bar{y}_s]}{\sum_{i=0}^{N-1}[y_s(t_i) - \bar{y}_s]^2}, \quad (10)$$

with $\bar{y}_s$ defined as the mean of $y_s(t_i)$. This function is found to peak at integer multiples of the period required for a particular feature to return to the same limb in subsequent rotations. In our case, the repeat period of the observed long-lived structures was determined from the ACFs of the O VI intensity time series. Long-term trends in the yearly data set were removed before estimation of the ACF. The autocorrelation procedure requires evenly sampled data. Since the set of N observations was unevenly distributed in time, the log-compressed time series data were resampled at N equispaced intervals by linear interpolation. Resampling of unevenly spaced data introduces a source of uncertainty in the period estimation by ACF techniques. Corrections for removing the sampling distortion have been proposed (e.g., Scargle 1989). However, a more detailed treatment of the data for period determination has already been widely discussed in § 3.1, and Monte Carlo simulations in order to verify the reliability of rotation period determination will be examined in detail in the Appendix. The ACF technique discussed in this section is just a complementary method that enables us both to double-check our results and to compare them (consistently) with those obtained with a similar autocorrelation analysis by Lewis et al. (1999) for white-light data in the same period. At each heliolatitude, defined as the heliographic latitude measured counterclockwise from the north pole, estimates of the centroids of the individual autocorrelation peaks were used to determine the period by dividing the lag at which they occurred by their recurrence number. Recurrence numbers identify the autocorrelation peak maxima, so that a recurrence number equal to n (= 0, 1, 2, . . .) corresponds to the autocorrelation peak at lag $n * T$ (= 0, T, 2T, . . .). Error estimates for the ACF peaks were evaluated as the square root of the estimated variance of the ACF, computed at the lags at which the peaks occurred, according to standard techniques (Bartlett 1946; Jenkins & Watts 1969). In order to have a reliable estimate of the synodic period, 18 period estimates per heliolatitude have been used, corresponding to the first nine peaks in the ACFs for both limbs. Finally, the weighted averages of these semi-independent estimates were taken (at each latitude) as the rotation period. In determining the weighted mean of our estimates, weights were assigned equal to the inverse of the estimated variances of the ACF peaks. Statistical errors of the periods were simply inferred by weighted standard deviation estimates.

4. RESULTS

4.1. *Latitudinal Variation*

The latitudinal variations of the rotation periods estimated by applying both the Lomb-Scargle periodogram and the autocorrelation techniques to the available set of data are shown, respectively, in the left and right panels of Figure 5. These results were obtained by analyzing the O VI 1032 Å spectral line time series with the instrumental slit height ranging from 1.5 through 2.0 $R_\odot$, covering a latitudinal region of about $\pm 60^\circ$ from the equator. As already mentioned, we emphasize that each angular position corresponds to slightly different heliocentric distances with respect to the nominal ones (refer to Table 1 for a quantitative estimate of this effect). Up to the uncertainties of both the autocorrelation and the Lomb-Scargle analysis (about 0.10–0.30 days per rotation period near the equator), the results from the two techniques applied to the same data set agree remarkably, both qualitatively and quantitatively. By averaging over a spatial region of $\pm 7^\circ$ around the equator, our best estimate for the equatorial rotation period of the corona at 1.50 $R_\odot$ is 27.48 $\pm$ 0.10 days with the Lomb-Scargle periodogram technique and 27.44 $\pm$ 0.13 days with the autocorrelation technique, in agreement with the $\pm 45^\circ$ latitude averaged coronal rotation determined by Lewis et al. (1999).

The variation of the coronal rotation with latitude at 1.5 $R_\odot$ shows that, as observed in the O VI 1032 Å emission line, the UV extended corona increases its rotation period from the equator up to the poleward boundary of the midlatitude streamers. The rotation period reaches a peak of 28.16 $\pm$ 0.20 days around 120° in the southern quadrant, while around 60° in the northern quadrant, at the symmetrical latitude with respect to the equator, there is a less evident peak at 27.57 $\pm$ 0.22 days. Over these peaks, toward the poles, the rotation period is seen to decrease again. At these higher latitudes, however, the period estimate is more problematic, due to both low signal-to-noise ratios and projection effects of lower latitude features out of the plane of the sky. The observed departure from rigid rotation is in agreement with the results of Stenborg et al. (1999) obtained using LASCO C1 data in the lower corona.

The observed latitudinal variation of the rotation period is also confirmed by results obtained from the analysis of the intensity time series of the H I Lyα 1216 Å spectral line. As shown in Figure 6, the period estimates from these two independent time series show good agreement at midlatitudes where, as already noted in previous works (e.g., Hansen et al. 1969), the rotational modulation is expected to be stronger than in the bright and almost time-independent equatorial streamer belt at solar minimum. In fact, in the equatorial region, the hydrogen scattering across the magnetic lines is large (see Fig. 2), and the period determination is affected by large errors and low periodicity significance. For these reasons, only the midlatitude periods from H I Lyα data are shown in Figure 6 for comparison with the O VI 1032 Å results. In the same figure, the UV coronal rotation as a function of latitude is compared with the differential sunspot groups rotation (Brajša et al. 2002). Although the overall coronal rotation is definitely more rigid, it appears to match the sunspot rotation in both hemispheres quite well in a region around $\pm 15^\circ$–25° from the equator while, closer to the equator, it appears to rotate slower than the sunspots. This result can be interpreted in terms of small-scale, but strong, magnetic fields linked to the sunspots influencing the rotation of the low plasma β coronal midlatitude plasma, at least at lower heights. The slower rotating regions at midlatitudes are also evident at higher distances (from 1.7 to 2.0 $R_\odot$). A careful inspection shows that although the values of the period peaks remain quite constant while getting away from the Sun, their positions tend to move toward lower latitudes with increasing distance. This behavior appears to track the helmet-like extensions of the low corona closed-loop systems, which are bent toward the equatorial plane, i.e., the dipolar-like structure of the global corona (see also Fig. 9).

4.2. *Radial Variation*

Previous investigations making use of white-light data from K-coronameters (e.g., Hansen et al. 1969), found a nearly constant rotation rate for heights ranging from about 1.1 to 2 $R_\odot$. However, recent radio observations seem to indicate that the rotation rate in the equatorial region actually decreases noticeably with height in the inner corona (Vats et al. 2001). By using a larger

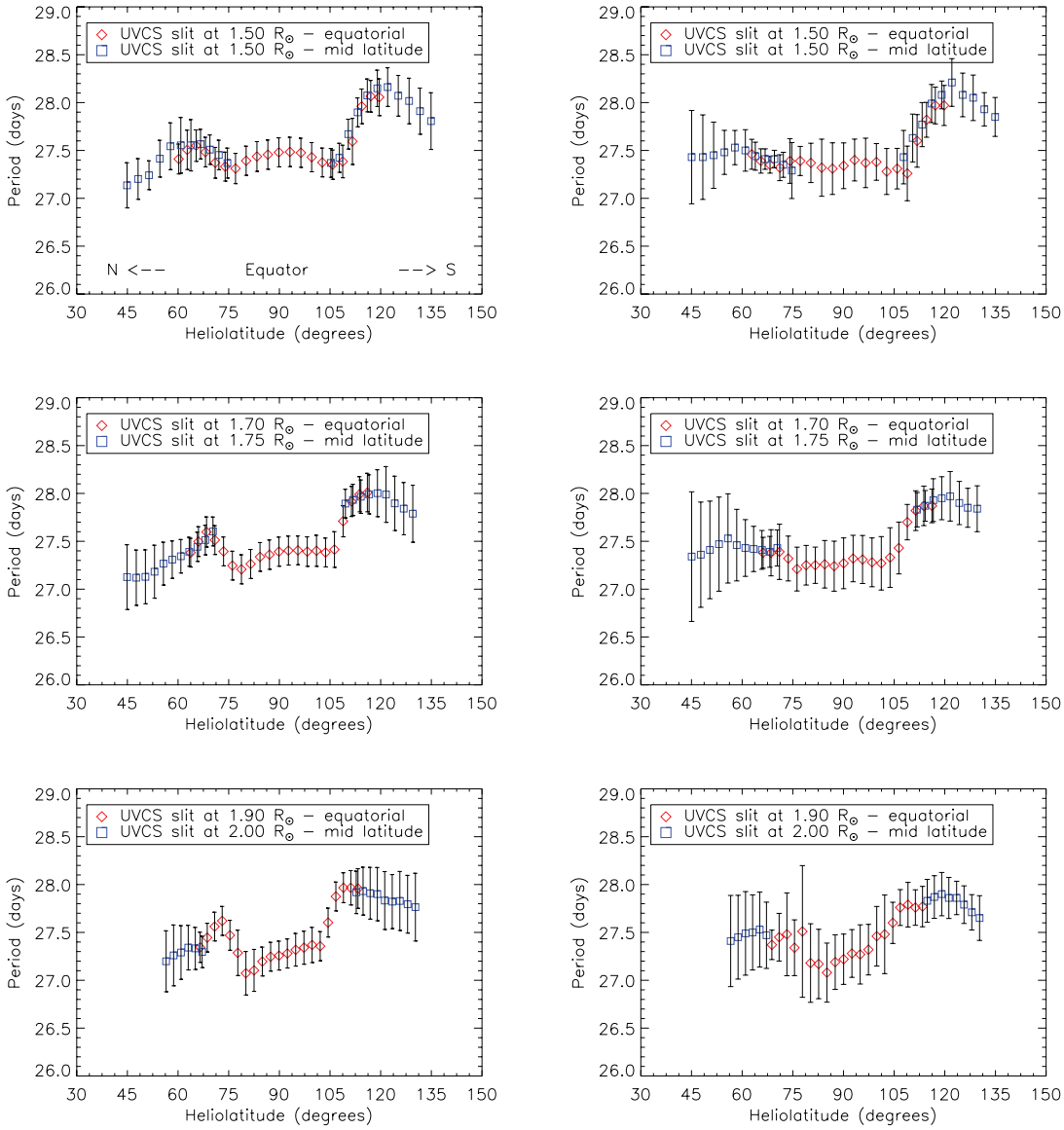

FIG. 5.—*Left*: Latitude dependence of the coronal rotation rate between 1.5 and 2.0 $R_\odot$ obtained with the Lomb-Scargle periodogram technique from the analysis of O VI 1032 Å time series. *Right*: Same as left, but obtained with the autocorrelation technique. The red and blue colored points represent the equatorial and midlatitudes pointings, respectively.

set of data, spanning from the inner to the outer corona, Lewis et al. (1999) found that the plasma in the inner corona, in particular below 2 $R_\odot$, tends to rotate at a slightly faster rate than the extended corona. The discrepancy is small, of order 1%, but was found in excess of the estimated systematic instrumental errors. In particular, LASCO C1 observations hint at a more or less constant period of 27.4 days much below 2 $R_\odot$, while between 2.5 and 5 $R_\odot$, LASCO C2 estimates look consistently higher (around 27.65 days) than the LASCO C1 ones (see Fig. 6 in Lewis et al. 1999). Lewis et al. (1999) could not constrain the radial gradient of rotation between the two coronal regions (inner and extended corona), due to a gap of several tenths of solar radii in the LASCO C1 and C2 fields of view around 2 $R_\odot$. Moreover, the above observations were obtained through two different telescopes and thus might have been affected by instrumental and systematic errors.

UVCS observations fill the gap between the inner and extended corona in the equatorial region. Our result, shown in Figure 7, obtained by averaging data of three spatial bins around the equator, supports the view that the observed discrepancy between the LASCO C1 and C2 rotation periods is *not* an artifact due to the different sensitivity (or systematic errors) of the two LASCO telescopes, but a real feature. The plot indicates that, at least in the equatorial region, the extended corona rotates slower than the inner corona. More precisely, the observed equatorial synodic rotation period is about 0.2 days period^{-1} shorter when the height increases from 1.5 to 2.3 $R_\odot$ (which is about 1% of the period), while it increases by 0.4 day period^{-1} (about 2%) between 2.3 and 2.5 $R_\odot$. The data, therefore, imply an abrupt transition between about 2.3 and 2.5 $R_\odot$, where the rotation rate is observed to slow down noticeably. In Figure 8, we show the gradient of the outward rotation period with height, together with 3 σ estimates of the associated errors, calculated by a linear fit to the first three available heights (say, between 1.5 and 2 $R_\odot$). In general, the average rotation periods in the inner corona (below about 2.3 $R_\odot$) decrease with height at low latitudes (within about 10° from the

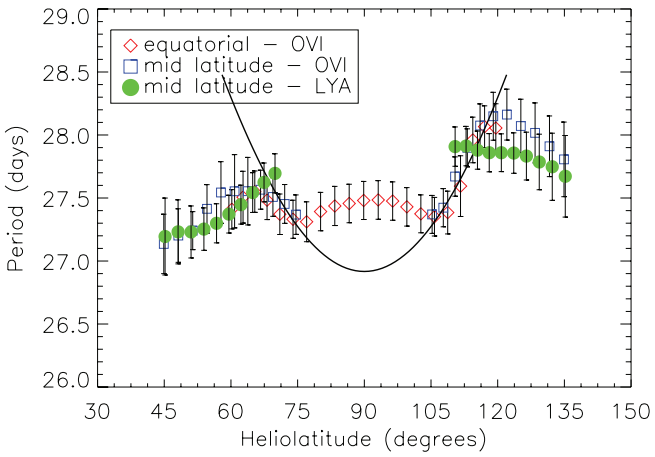

FIG. 6.—Comparison of the coronal rotation period at 1.5 $R_\odot$ obtained with the Lomb-Scargle periodogram technique from the O VI 1032 Å (*red and blue*) and H I Lyα (*green*) time series. The solid line shows the differential rotation period for recurrent sunspot groups near the solar minimum obtained by Brajša et al. (2002).

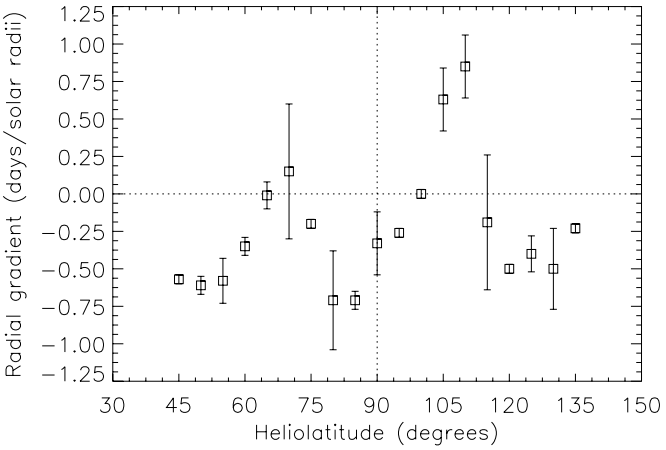

FIG. 8.—Radial gradient of the coronal rotation period in the inner corona (lower than 2 $R_\odot$) with 3 σ estimates of the associated errors.

solar equator) and high latitudes (above about 30° from the solar equator) and increase with height about 20° above and below the solar equator, which roughly corresponds to the transition region between the streamer belt plasma and the coronal hole boundaries.

As for the interpretation of the quasi-rigid rotation of the coronal plasma, it seems difficult to reconcile the presence of differential rotation of magnetic fields at the photosphere level with almost rigid rotation of coronal structures ultimately related to the same fields. According to Billings (1966) and Pneuman (1971), individual loop structures connecting high and low latitudes might enforce a more rigid rotation above the photosphere, although this mechanism would not resolve the problem that open field lines emanating from the coronal poles also rotate quite rigidly. Alternatively, it has been speculated that the coronal large-scale magnetic features are anchored to deeper layers within the more rigidly rotating interior of the Sun (Stenflo 1977; Zirker 1977).

4.3. *North-South Asymmetry*

Asymmetries between the northern and southern hemisphere were previously found in the rotation velocities of photospheric magnetic fields (Antonucci et al. 1990; Javaraiah & Gokhale 1997). For example, it has been found that the northern hemisphere rotates faster during even cycles (20 and 22), while the rotation of the southern hemisphere dominates in odd ones (cycles 19 and 21; Gigolashvili et al. 2005), a property that has been also interpreted with theoretical arguments (Itoh et al. 2005).

A strong asymmetry in the rotation of the north and south hemispheres is also noticeable in Figures 5 and 9. In particular, in the northern hemisphere, the rotation looks more solid-body–like (within the errors), while the rotation rate is noticeably slower in the southern hemisphere. This asymmetry might indicate a weak coupling between the magnetic fields of the two hemispheres. In fact, several studies (e.g., Joshi et al. 2006 and references therein) reveal the existence of a real asymmetry in the occurrence of various features of solar activity (such as flares, sunspot numbers, sunspot areas, prominences/filaments, magnetic flux, and coronal intensity) that have bearing on the solar

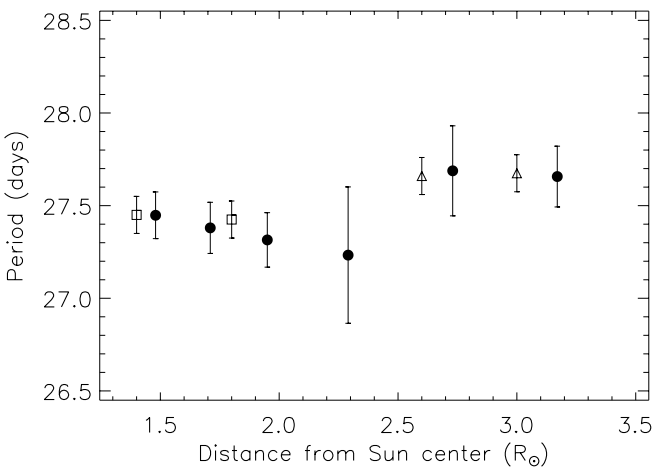

FIG. 7.—Radial dependence of the rotation period around the solar equator. Filled circles show the results from UVCS data, while open squares and triangles denote, respectively, the period estimates from LASCO C1 and C2 observations (Lewis et al. 1999).

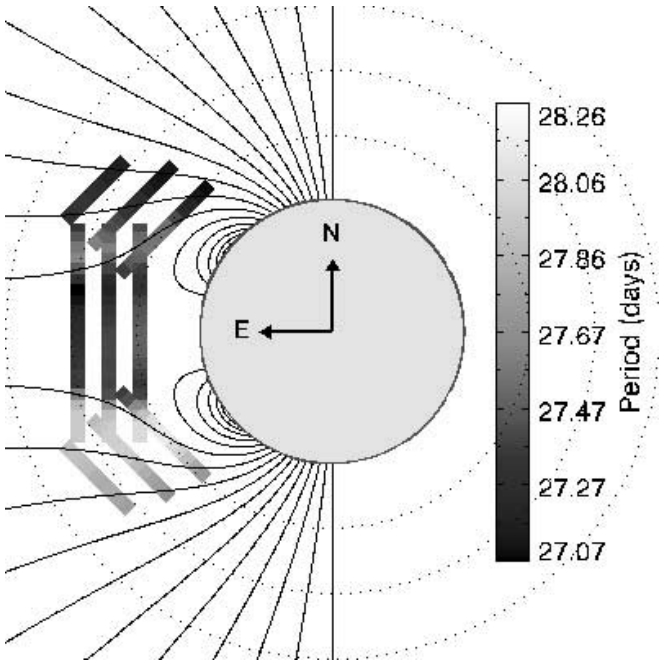

FIG. 9.—Color-scale representation of the computed synodic rotation period in the coronal region from 1.48 to 2.23 $R_\odot$ and ±60° around the equator, with, superimposed, a coronal magnetic field model (Banaszkiewicz et al. 1998). [*See the electronic edition of the Journal for a color version of this figure.*]

dynamo mechanism (Ossendrijver et al. 1996) and may be due to phase differences between the magnetic activity in both hemispheres (Swinson et al. 1986; Waldmeier 1971). Anticorrelation between rotation and activity is proven to exist not only in time (during an activity cycle), but also in space, with the more active hemisphere rotating slower (Obridko & Shelting 2001). An increased activity is thus seen to be accompanied by a decreased rotation rate and, vice versa, the higher the rotation rate, the lower the activity. In agreement with the above studies, our results also show that, at the start of cycle 23, the more active hemisphere, the southern one (Zharkov et al. 2005), rotates somewhat slower.

5. DISCUSSION AND CONCLUSIONS

We have used synoptic UVCS observations to establish the rotational characteristics of the solar corona at the minimum of solar activity in the time interval from 1996 May to 1997 May. The capabilities of UVCS allow estimating of coronal rotational rates, from a minimum height of 1.5 to about 3 $R_\odot$, by studying the recurrence of persistent structures. The results were reproduced with two independent computational procedures, the Lomb-Scargle periodogram method and the more traditional autocorrelation technique, in order to verify that conclusions were not affected by the specific technique employed.

The coronal rotation rates obtained in this study confirm already established results that the corona, during minimum activity, tends to rotate with a less pronounced differential rotation than the plasma of the photosphere. Moreover, we found a deceleration of the corona toward the photospheric rates at midlatitudes, where localized flux concentrations of the new-cycle active regions are emerging. This evidence suggests that the corona can be broadly affected by localized flux concentrations (e.g., Weber et al. 1999) and that the slower rotation periods can be related to the active regions, that is, to the short-lived features, while the faster components can be related to the large-scale global magnetic field.

The study of the radial variation of the coronal rotation period shows that the average rotation periods increase with height at the latitudes that roughly correspond to the transition region between the streamer belt plasma and the coronal hole boundaries at solar minimum (about 20° above and below the solar equator). Moreover, in the equatorial region the rotation, which seems to be more strictly influenced by the coronal large-scale global magnetic field structure, is almost rigid, but the observed equatorial synodic rotation period shows an abrupt increase of about half a day between 2.3 and 2.5 $R_\odot$, where the coronal plasma starts to be dominated by the open field lines extending to the heliosphere. In Figure 9, a plausible solar minimum magnetic field configuration, here described by the analytical dipole-quadrupole current sheet model developed by Banaszkiewicz et al. (1998), is superimposed on the map of coronal rotation periods obtained from our data. By visual inspection, the radial and latitudinal profiles of the coronal rotation seem to track the magnetic topology fairly well. In particular, the larger gradients of the rotation rates are localized at the boundary between the open and closed field lines, where the differential photospheric rotation is somehow translated to the corona, as also observed by Stenborg et al. (1999). It is intriguing that the larger rotation gradients, observed at the midlatitudes and around 2.5 $R_\odot$ at the equator, might be related to the boundary regions, which have been identified with the locations where the slow solar wind originates (e.g., Antonucci et al. 2005; Noci & Gavryuseva 2007), and to the regions where small transients are released near the cups of helmet streamers (Sheeley et al. 1997). The observational evidence suggests possible magnetic shears as a consequence of the rotation profile variation with latitude and distance. In particular, the steep gradient around 2.5 $R_\odot$ can drive a magnetic reconfiguration and thus, a possible energy release to heat the corona, as discussed, for example, by Lewis et al. (1999) and Simnett (1994). Since at solar maximum the magnetic field configuration is more complex and rapidly changing, the streamer boundaries, where we observed the rotation rate variation at solar minimum, are more difficult to localize. Therefore, we expect a more uniform coronal rotation from the analysis of the UVCS data available at the time of the maximum of solar activity.

Summarizing, we were able to describe the latitudinal and radial variation of the solar corona rotation from 1.5 to about 3 $R_\odot$. Our results are in general agreement with the ones from previous investigations. At solar minimum, we find evidence of a differential rotation in the UV solar corona significantly different from that of the photosphere. In particular, our best estimate for the equatorial rotation period of the corona at 1.5 $R_\odot$ is 27.48 ± 0.10 days with the Lomb-Scargle periodogram technique and 27.44 ± 0.13 days with the autocorrelation technique. The variation of the coronal rotation with latitude at 1.5 $R_\odot$ shows that the UV corona increases its rotation period from the equator up to the poleward boundary of the midlatitude streamers, reaching a peak of 28.16 ± 0.20 days around 120° in the southern quadrant and a peak of 27.57 ± 0.22 days around 60° in the northern quadrant. These results suggest the presence of a real asymmetry between the northern and southern coronal rotation rates, indicating a weak coupling between the magnetic fields of the two hemispheres. Finally, we found that the radial and latitudinal profiles of the coronal synodic rotation period show departures from rigid rotation in the region where the slow solar wind and small transients originate, thus suggesting that in these regions the steep gradients of the rotation rates might be a source of magnetic stress and, consequently, of energy release.

We wish to thank Ester Antonucci for suggesting and encouraging the coronal rotation study by means of UVCS data. We thank Claudia Raiteri for helpful discussion on data series analysis techniques and the anonymous referee for his/her careful and constructive comments on our manuscript. This research has been supported by contract ASI/I/035/05/0 of the Italian Space Agency (ASI). *SOHO* is a project of international cooperation between the European Space Agency (ESA) and the National Aeronautics and Space Administration (NASA). UVCS is a joint project of NASA, ASI, and the Swiss Funding Agencies.

APPENDIX

In this appendix, we describe in detail the Monte Carlo simulations that were used in this paper to verify the reliability of rotation period determination by means of Lomb-Scargle periodograms applied to the time series obtained from UVCS coronal observations. In particular, in order to reject the possibility that the periods found in our analysis could be artifacts due to noise or sampling effects, we ran simulation studies for the time series presented in Figures 3 and 4 that were measured, respectively, at 90° and 120° from north pole.

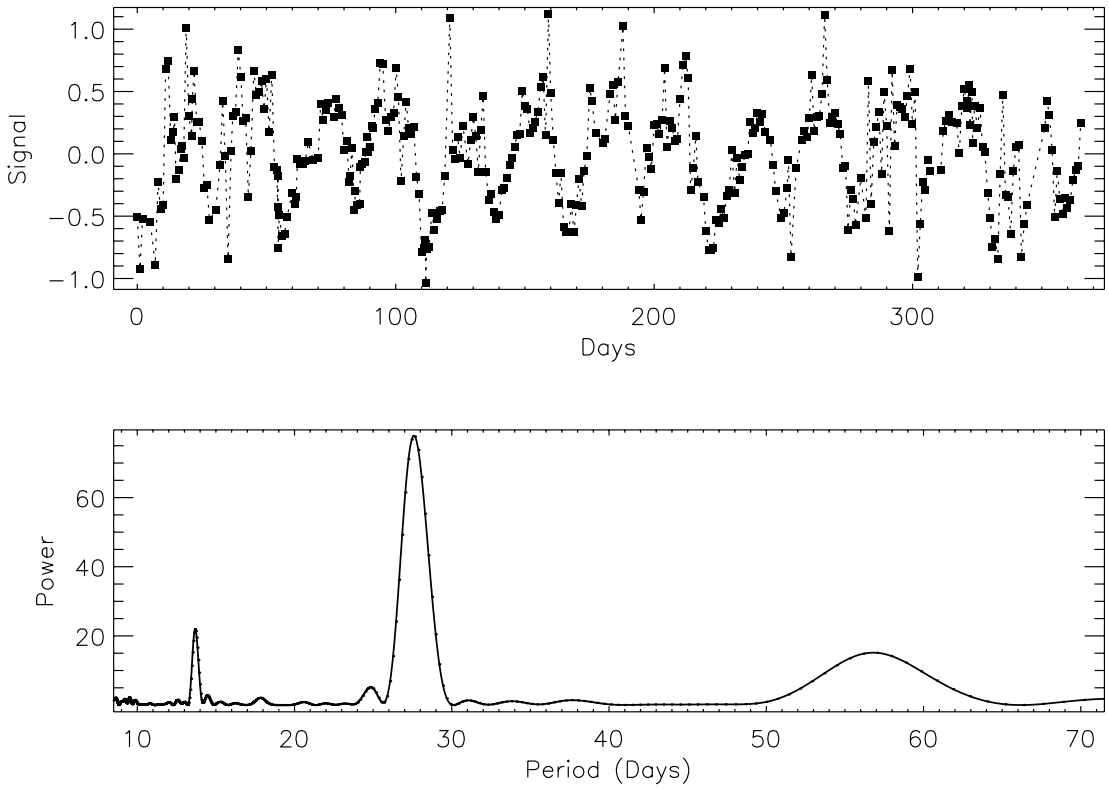

FIG. 10.—*Top*: Example of a periodic signal realization, $s'(t_i)$, in which the signal contains sinusoids at the main rotation period and its harmonics and the random noise is taken from a Gaussian distribution of the "residuals," r_i (see text). *Bottom*: Power spectrum obtained from the Lomb-Scargle analysis. The main period and its harmonics are evident.

A first simulation (test A) was run using the Lomb-Scargle method to determine the rotation periods over a large number of realizations of the time series that were modified by adding a noise signal, sampled from a Gaussian distribution, with standard deviation given by the difference between the real data points and the sinusoidal data fit at the estimated period. In what follows, we describe in detail the procedure that was used to perform test A. After inferring the period of the true time series, p, using the Lomb-Scargle technique, a sinusoidal least-squares fit, $y_i = A \sin[(1/p)t_i + \phi] + b$, with $i = 1, \ldots, N$, was computed from the data, and the "residuals," r_i, defined as the absolute differences between the observed and the fitted values, $r_i = \left[(f_i - y_i)^2\right]^{1/2}$, were inferred to estimate the uncertainties. A continuous periodic signal, $s(t)$, containing sinusoids at the main rotation period and its harmonics, was then created, and a simulated signal, $s'(t_i) = s(t_i) + n_i$, was extracted from it. Here $s(t_i)$ denotes the sampling of $s(t)$ at the times t_i and the n_i are random noise samples from Gaussian distributions with standard deviations r_i. An example of simulated signal is shown in the top panel of Figure 10. We ran 20,000 realizations of the random noise and, for each one, we determined the rotation period, $p_{\rm sim}$, by applying the Lomb-Scargle technique on the simulated data, $s'(t_i)$. A typical power spectrum is shown in the bottom panel of Figure 10.

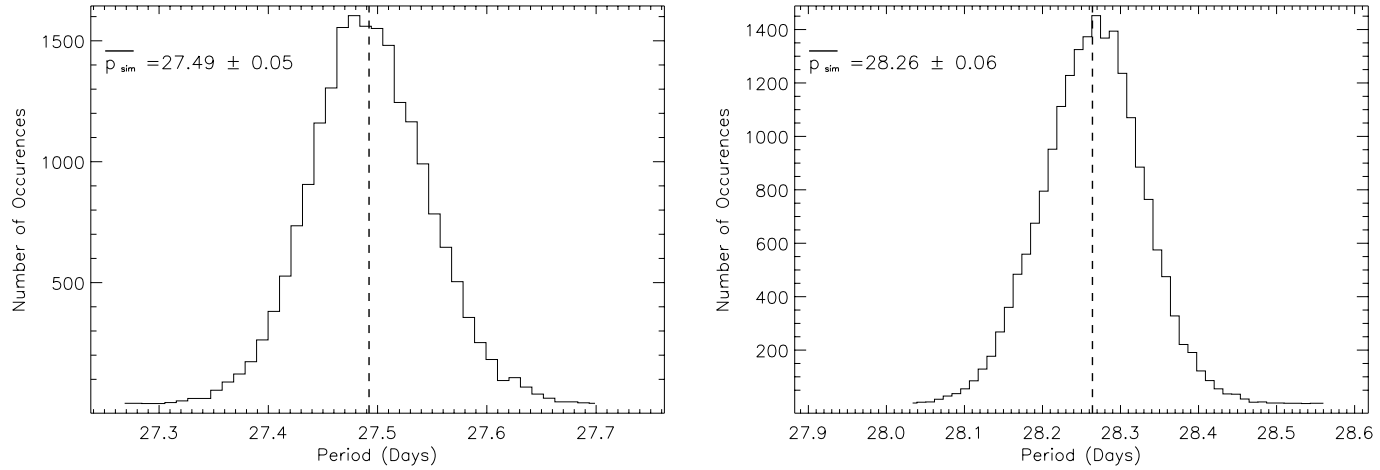

FIG. 11.—Simulated period distribution for test A. *Left*: Results for the time series at 90° reported in Fig. 3. *Right*: Results for the time series at 120° reported in Fig. 4.

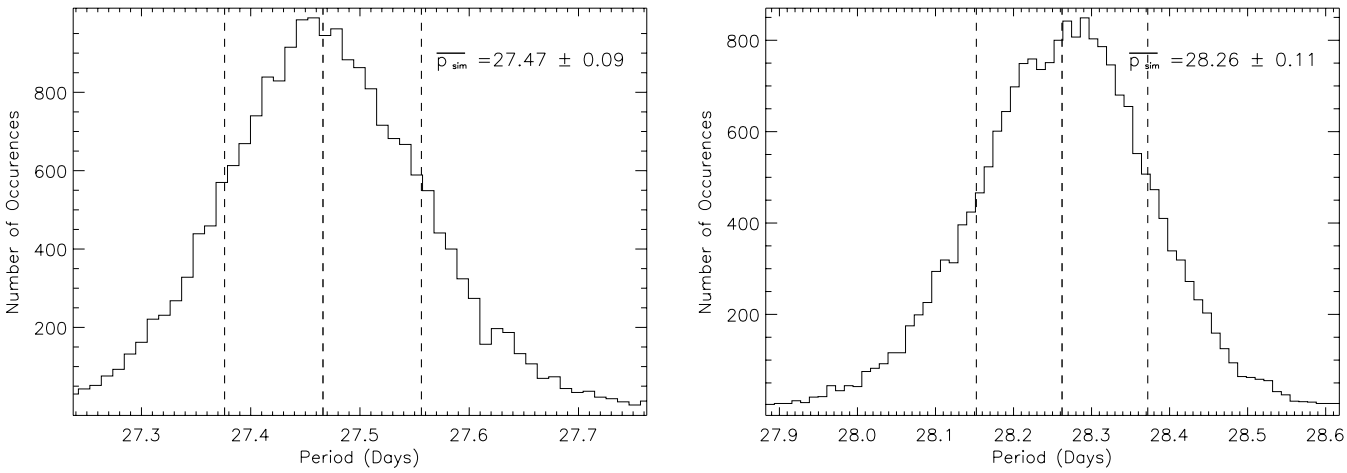

FIG. 12.—Simulated period distribution for test B. *Left*: Results for the time series at 90° reported in Fig. 3. *Right*: Results for the time series at 120° reported in Fig. 4.

Finally, from the distribution of the rotation periods, we found the average simulated rotation period, $\overline{p}_{\rm sim}$, and its uncertainty. The same test was also run by adding the true uncertainties instead of the "residuals."

A second simulation (test B) was designed following the method suggested by Peterson et al. (1998). In this test, the time series were randomized with a noise given by the measurement uncertainties, and only a random subset of the data points was selected. This latter method allows assessing the uncertainties in the period determination associated with the uncertainties in individual measurements and with the observation sampling. In what follows, we describe in detail the procedure used to perform test B. After inferring the period of the true time series, p, using the Lomb-Scargle technique, we applied the so-called flux randomization (Peterson et al. 1998), which consists of altering the measured fluxes, f_i, by adding random noise, $f_i' = f_i + n_i$, where n_i are random noise samples from Gaussian distributions with standard deviations σ_i. After the flux randomization, N data points were randomly selected, and the redundant data points were excluded, thus reducing the number of data by a factor of $1/e$, the Poisson probability of not selecting any particular point. A data realization f_j'' was then defined, with $j = 1, \ldots, NN$, where $NN \simeq N/e$. We ran 20,000 realizations of f_j'', and for each one we determined the rotation period, $p_{\rm sim}$, using the Lomb-Scargle technique. Finally, we computed the distribution of the rotation periods obtained from the simulated data. Then we quoted the period, p, as the median of the distribution and the uncertainty, $\sigma_{\rm sim}$, defined such that 68.27% of the realizations yield results in the range $p \pm \sigma_{\rm sim}$, corresponding to 1 σ errors for a normal distribution (Peterson et al. 1998).

The rotation period distributions obtained by means of the aforementioned Monte Carlo simulations (tests A and B) of the time series at 90° and 120° are reported, respectively, in Figures 11 and 12. Results for both tests are summarized in Table 3, together with estimates of the period inferred from the real time series. In all cases, the periods inferred from the simulated data are clearly consistent with those estimated from the observed data. We point out, however, that the uncertainties determined from test B are larger than those from test A and close to the values computed with equation (8). This is because test B takes into account the two main sources of uncertainties, that is, the uncertainties in individual measurements and those associated with the observational sampling.

Finally, we designed a Monte Carlo simulation to test the statistical significance of the secondary peaks that often appear near the main peak (see, for example, the peak around 32 days in Fig. 4) in order to verify whether they represent real features (minor periods) or aliases due to data sampling. To this end, we performed again test A and sought for all the relative maxima of the periodograms obtained from the time series shown in Figures 3 (obtained at latitude 90°) and 4 (obtained at latitude 120°). For a large number of representations of a fictitious signal containing both a known sinusoid and its harmonics (plus a random noise estimated from the real data), we found all the peaks. In Figure 13, we display the power of all the relative periodogram maxima that were found for both the 90° (*left*) and the 120° (*right*) time series, respectively. As expected, the highest peaks appear at the respective input periods (27.46 and 28.27 days) and at their harmonics. However, we also find lower peaks, around the main period, at values similar to those observed in the periodogram obtained from the analysis of the true data set (see Figs. 3 and 4). These secondary peaks, however, have low significance and never exceed the 0.1% significance level, which has been assumed as a significance threshold for the rotational periods inferred in this paper. We thus infer that the subsidiary peaks often observed near the main period are attributable to the effect of sidelobes in the spectral estimator due to the finite length of the data window and to spectral leakage from the input period (e.g., Scargle 1982).

TABLE 3
RESULTS OF MONTE CARLO SIMULATIONS

Roll (deg)	True Data p (days)	Test A $\overline{p}_{\rm sim}$ (days)	Test B $\overline{p}_{\rm sim}$ (days)
90	27.46 ± 0.11	27.49 ± 0.05	27.47 ± 0.09
120	28.27 ± 0.13	28.27 ± 0.06	28.26 ± 0.11

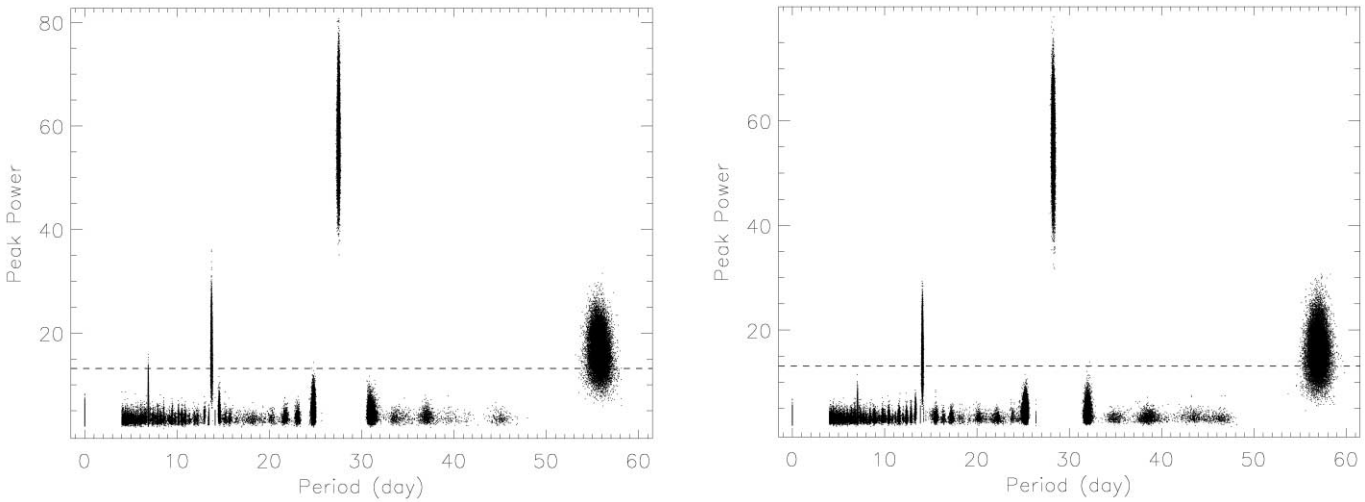

FIG. 13.—Power of all the relative periodogram maxima from simulated sinusoidal signals with the main period at 27.46 days (*left*) and 28.27 days (*right*). The horizontal dashed lines represent the 0.1% significance level, which has been assumed as a significance threshold for the rotational periods inferred in this paper. It is evident that only the periods present in the simulated data and its harmonics have powers higher than that threshold.

REFERENCES

Antonucci, E., Abbo, L., & Dodero, M. A. 2005, A&A, 435, 699
Antonucci, E., Hoeksema, J. T., & Scherrer, P. H. 1990, ApJ, 360, 296
Antonucci, E., & Svalgaard, L. 1974, Sol. Phys., 34, 3
Aschwanden, M. J., Lim, J., Gary, D. E., & Klimchuk, J. A. 1995, ApJ, 454, 512
Banaszkiewicz, M., Axford, W. I., & McKenzie, J. F. 1998, A&A, 337, 940
Bartlett, M. S. 1946, J. Royal Statistical Soc., B8 Suppl., 27
Billings, D. E. 1966, A Guide to the Solar Corona (New York: Academic)
Box, G. E. P., & Cox, D. R. 1964, J. Royal Statistical Soc., Ser. B, 26, 211
Brajša, R., et al. 2002, Sol. Phys., 206, 229
Cora, A., Antonucci, E., Dimitoglou, G., Volpicelli, C. A., & Giordano, S. 2003, Mem. Soc. Astron. Italiana, 74, 819
Fisher, R., & Sime, D. G. 1984, ApJ, 287, 959
Gigolashvili, M. S., Japaridze, D. R., Mdzinarishvili, T. G., & Chargeishvili, B. B. 2005, Sol. Phys., 227, 27
Giordano, S. 1998, Ph.D. thesis, Univ. Torino
Hansen, R. T., Hansen, S. F., & Loomis, H. G. 1969, Sol. Phys., 10, 135
Hoeksema, J. T., & Scherrer, P. H. 1987, ApJ, 318, 428
Horne, J. H., & Baliunas, S. L. 1986, ApJ, 302, 757
Itoh, S.-I., Itoh, K., Yoshizawa, A., & Yokoi, N. 2005, ApJ, 618, 1044
Javaraiah, J., & Gokhale, M. H. 1997, Sol. Phys., 170, 389
Jenkins, G. M., & Watts, D. G. 1969, Spectral Analysis and Its Applications (London: Holden-Day)
Joshi, B., Pant, P., Manoharan, P. K., & Pandey, K. 2006, in ASP Conf. Ser. 368, ed. P. Heinzel, I. Dorotovič, & R. J. Rutten (San Francisco: ASP), 539
Kohl, J. L., et al. 1995, Sol. Phys., 162, 313
Lewis, D. J., et al. 1999, Sol. Phys., 184, 297
Lomb, N. 1976, Ap&SS, 39, 447
Mancuso, S., & Garzelli, M. V. 2007, A&A, 466, L5
Noci, G., & Gavryuseva, E. 2007, ApJ, 658, L63
Noci, G., et al. 1997, in Proc. Fifth *SOHO* Workshop, The Corona and Solar Wind near Minimum Activity, ed. A. Wilson (ESA SP-404; Noordwijk: ESA), 75
Obridko, V. N., & Shelting, B. D. 2001, Sol. Phys., 201, 1
Ossendrijver, A. J. H., Hoyng, P., & Schmitt, D. 1996, A&A, 313, 938
Park, S., & Schowengerdt, R. 1983, Comput. Vision, Graphics & Image Processing 23, 256
Parker, G. D., Hansen, R. T., & Hansen, S. F. 1982, Sol. Phys., 80, 185
Peterson, B. M., et al. 1998, PASP, 110, 660
Pneuman, G. W. 1971, Sol. Phys., 19, 16
Press, W. H., & Rybicki. G. B. 1989, ApJ, 338, 277
Press, W. H. Teukolsky, S. A., Vetterling, W. T., & Flannery, B. P. 2007, Numerical Recipes: The Art of Scientific Computing (3rd ed.; Cambridge: Cambridge Univ. Press)
Ranucci, G. 2006, Phys. Rev. D, 73, 103003
Scargle, J. D. 1982, ApJ, 263, 835
———. 1989, ApJ, 343, 874
Sheeley, N. R., et al. 1997, ApJ, 484, 472
Sime, D. G., Fisher, R. R., & Altrock, R. C. 1989, ApJ, 336, 454
Simnett, G. M. 1994, Space Sci. Rev., 70, 69
Stenborg, G., Schwenn, R., Inhester, B., & Srivastava, N. 1999, in Proc. Magnetic Fields and Solar Processes, The 9th European Meeting on Solar Physics, ed. A. Wilson (ESA SP-448; Noordwijk: ESA), 1107
Stenflo, J. O. 1977, A&A, 61, 797
Swinson, D., Koyama, H., & Saito, T. 1986, Sol. Phys., 106, 35
Vats, H. O., Cecatto, J. R., Mehta, M., Sawant, H. S., & Neri, J. A. C. F. 2001, ApJ, 548, L87
Waldmeier, M. 1971, Sol. Phys., 20, 332
Wang, Y.-M., et al. 1997, ApJ, 485, 875
Weber, M. A., Acton, L. W., Alexander, D., Kubo, S., & Hara, H. 1999, Sol. Phys., 189, 271
Zharkov, S., Zharkova, V. V., & Ipson, S. S. 2005, Sol. Phys., 228, 377
Zirker, J. B. 1977, Rev. Geophys. Space Phys., 15, 257